ELSEVIER

Journal of Fluids and Structures 20 (2005) 483–503

JOURNAL OF FLUIDS AND STRUCTURES

www.elsevier.com/locate/jfs

Vortex mode selection of a rigid cylinder subject to VIV at low mass-damping

D. Lucor, J. Foo, G.E. Karniadakis*

Center for Fluid Mechanics, Turbulence and Computation, Division of Applied Mathematics, Brown University, Providence, RI 02912, USA

Received 12 October 2004; accepted 14 February 2005
Available online 12 May 2005

Abstract

We present direct numerical simulations results of vortex-induced vibrations of a freely vibrating rigid cylinder with low mass-damping parameter using a spectral/*hp* element method. We investigate several reduced velocities to assess the validity of the ''three-branch response'' and its sensitivity to Reynolds number in the range 1000–3000. This study addresses the numerical challenge of capturing large amplitude responses in the upper branch and the 2P vortex shedding mode in the lower branch, which has been observed in experiments. We focus, in particular, on the region of reduced velocities around the mode transition between the upper and the lower branch of response. In this region, there exists a sharp drop in the spanwise correlation of the wake and forces, which, surprisingly, does not diminish the response of the cylinder. Therefore, detailed measurements of the phasing along the span are crucial to understanding the system and its mechanism for vortex mode selection. We use complex demodulation analysis to quantify the spatio-temporal phase relationship between the forces and cylinder displacement. We also compute the correlation length of the forces along the span of the cylinder.

Keywords: Free vibrations; Turbulent wakes; Direct numerical simulation

1. Introduction

The study of vortex-induced vibrations (VIV) of an elastically mounted rigid cylinder with low mass-damping parameter constrained to move transversely to a uniform flow remains of practical and theoretical importance. The distinction between the three response branches (see Fig. 1) arising in different ranges of the nominal reduced velocity V_{rn} has been described in the literature (Khalak and Williamson, 1999; Govardhan and Williamson, 2000; Hover et al., 1998; Williamson and Govardhan, 2004). For low reduced velocities, there exists an *initial* branch associated with a 2S vortex shedding mode (two single vortices shed per cycle) and the mean forces and cylinder response are in phase. For intermediate and larger reduced velocities there exists an *upper* and a *lower* branch associated with a 2P vortex shedding mode (Khalak and Williamson, 1999; Govardhan and Williamson, 2000) (two pairs of vortices shed per cycle). However, very few three-dimensional numerical results have been able to accurately reproduce the three-branch response model obtained from experiments. Some have successfully predicted the 2P shedding mode in the lower branch

*Corresponding author. Tel.: +1 401 863 1217; fax: +1 401 863 3369.
E-mail address: gk@dam.brown.edu (G.E. Karniadakis).

0889-9746/$ - see front matter © 2005 Elsevier Ltd. All rights reserved.
doi:10.1016/j.jfluidstructs.2005.02.002

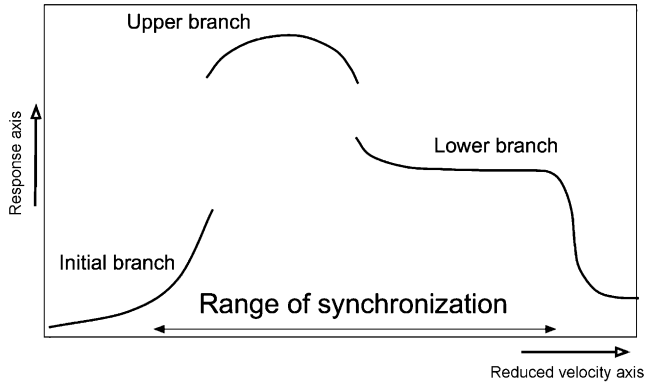

Fig. 1. Sketch of the "three-branches" response model.

(Blackburn et al., 2000), but this result has only been observed at large mass-damping parameters, small aspect ratio and moderate Reynolds number. In general, the task of capturing numerically the large amplitude response of the upper branch for low mass-damping systems with large aspect ratio has remained out of reach.

Another phenomenon, well-known by experimentalists, is the phase lag between the mean forces and cylinder response in the lower branch. However, the mechanisms that induce the phase jump during the transition from the *upper* to the *lower* branch are not well understood. The complexity of the phenomenon has possibly been overlooked and oversimplified in some experimental work, due to insufficient spanwise sampling. In particular, some studies indicate the existence of a reduced velocity region, containing the Strouhal frequency, for which a sharp drop in the spanwise correlation of the flow quantities in the wake and the forces is observed (Hover et al., 1998, 2004; Lucor et al., 2003). This region stands mainly on the end of the *upper* branch (and the loss of correlation does not diminish the response amplitude) near the transition between the *upper* and the *lower* branch (small amplitude response). The study of the phasing between cylinder displacement and forces in this region is key to the understanding of the mode transition.

In the present study, we perform direct numerical simulations (DNS) of a uniform flow past a rigid cylinder with low mass-damping parameter and aspect ratio 26 subject to VIV. The cylinder is free to move in the cross-flow direction but is constrained in the streamwise direction. We consider a Reynolds number range $\mathrm{Re} = 1000-3000$ and reduced velocity range $V_{rn} = 3.76-8.0$. We aim to:

(i) study the cylinder response, assess the validity of the "three-branch response" and quantify its sensitivity to Reynolds number;
(ii) investigate the existence and persistence of the 2P vortex shedding mode in the lower branch region; this task is achieved by performing flow visualizations of the near wake as well as frequency analysis;
(iii) assess the existence of a reduced velocity region, close or containing the Strouhal frequency, which exhibits poor spanwise correlation of forces but large response amplitudes;
(iv) quantify the three-dimensional effects that take place within this region of poor correlation using correlation length computations and complex demodulation phase analysis.

In the next section, we define our simulation parameters and go over the numerical post-processing techniques and analysis used in this work. In Section 3, we present amplitude response results. Then, we detail the different vortex synchronization patterns in Section 4. In Section 5, we present phasing analysis results. Finally, we conclude with the summary of our findings.

2. Simulation parameters and formulation

We present DNS results of VIV of a smooth rigid cylinder with aspect ratio $L/D = 26$ and mass ratio $m = 2$. We set the structural damping to be zero as we are interested in the maximum response of the system. This choice of mass ratio and structural damping corresponds to a low mass-damping parameter range. The Reynolds number is taken to be

$\mathrm{Re} = 1000$, 2000 and 3000. We only consider the dominant motion in the cross-flow direction, thus prohibit any motion of the structure in the streamwise direction. The governing equations are the incompressible Navier–Stokes equations coupled with the structural dynamical equation. The cylinder is represented by a single degree of freedom, i.e., the damped second-order oscillator subject to the external hydrodynamic forcing. The coupled Navier–Stokes/structure dynamics equations are discretized in space using a spectral/*hp* element method (Karniadakis and Sherwin, 1999) with a boundary fitted coordinate system. The method employs an unstructured hybrid grid with *hp* refinement in the (x, y) cross-plane and Fourier expansions in the z-direction (cylinder axis) with a dealiasing $\frac{3}{2}$ rule. Therefore, periodicity of the solution along the z-axis is implied. The origin of the coordinates is located at one end of the cylinder and lies on the cylinder axis. Variable spectral order is used for each element, which gives variable p-refinement between regions of different flow dynamics (Evangelinos and Karniadakis, 1999). This increase in Reynolds number, compared to previous work (Evangelinos, 1999; Evangelinos and Karniadakis, 1999), was made possible by advances in computer hardware [an increase of the Re by a factor two approximately requires one order of magnitude increase in CPU resources (Karniadakis and Orszag, 1993)], and also by the use of a larger and more refined grid (more than twice the number of elements compared to previous works). The thickness of the first layer of quadrilateral elements around the cylinder is $\delta = 1.25\%$ of the diameter D instead of $\delta = 3.5\%D$ in previous work (Evangelinos, 1999; Evangelinos and Karniadakis, 1999). This h-refinement (combined with a p-refinement) is sufficient to resolve the cylinder's boundary layer within the first layer of elements. Computations for $\mathrm{Re} = 3000$ were done with both 64 and 128 grid points along the spanwise direction in order to assess the sensitivity of the response to a change in the spanwise resolution.

2.1. Complex demodulation analysis

Multi-frequency responses and beating phenomena require a time-varying description of the phase difference between the cylinder displacement and the lift force. To quantify the phase difference we employ *complex demodulation analysis*, which is a generalized harmonic analysis, in dealing with nonexact periodic time series (Bloomfield, 1976). A complex demodulation of a time series $C_L(t_n, z)$ (lift coefficient time series at location z in the spanwise direction) with a dominant frequency component λ_{C_L} will output a time varying amplitude $R_{C_L}(t_n, z)$ and phase $\Phi_{C_L}(t_n, z)$ such that

$$C_L(t_n, z) \approx R_{C_L}(t_n, z)\mathrm{e}^{\mathrm{i}(\lambda_{C_L} t_n + \Phi_{C_L}(t_n,\, z))}. \tag{1}$$

The time-dependent amplitude and phase of the signal at time t are determined only by the portion of the signal in the neighborhood of t. The procedure uses linear filtering, which may be tuned by choosing some free parameters that control the width and the shape of the filter. Two frequencies need to be provided in addition to the frequency at which to demodulate the series. Those are the pass frequency λ_{pass} and the stop frequency λ_{stop} of the low-pass filter, respectively. The cut-off of the filter is half-way between λ_{pass} and λ_{stop}, so that the total number of terms in the filter is $n_{\mathrm{filter}} = \mathrm{floor}(2 \times \max(2, \lambda_{C_L}/(\lambda_{\mathrm{stop}} - \lambda_{\mathrm{pass}})) + 1)$. This process is repeated for the time series at each z-location along the span. Similarly, we would have for the cylinder displacement:

$$\eta(t_n) \approx R_\eta(t_n)\mathrm{e}^{\mathrm{i}(\lambda_\eta t_n + \Phi_\eta(t_n))}. \tag{2}$$

We note that we have no z-dependence because the cylinder is rigid. We define the phase difference $\Delta\Phi$ as

$$\Delta\Phi(t_n, z) = \Phi_\eta(t_n) - \Phi_{C_L}(t_n, z). \tag{3}$$

2.2. Correlation length

The fluctuations of the forces acting on the cylinder depend on the degree of three dimensionality present in the near-wake of the body. The spanwise correlation length of the flow gives an accurate measure of this three dimensionality, and thus some indication of the magnitude of the cylinder response amplitude. Experimental studies have been limited so far in terms of force measurements. While the resolution of experimental wake velocity measurements can compare favorably with DNS (Mansy et al., 1994), force measurements are limited to a few locations: the ends of the cylinder (Govardhan and Williamson, 2000; Hover et al., 1998) or on a two-dimensional slice (West and Apelt, 1993; Ribeiro, 1992) (stationary cylinder). The autocorrelation force profiles are usually much smoother than their corresponding velocity profiles in the wake. This is due to the integrated nature of the forces, and it results in larger correlation lengths (Lucor et al., 2003). Computing the time-averaged correlation length might mask some of the fluctuations of the flow quantities in time. Therefore, in the case of multi-frequency response or beating phenomena, short time integration of the correlation coefficient or phase drift angle analysis are necessary. For this problem, we define our autocorrelation

function as follows:

$$R(l,t)=\frac{1}{N_t}\sum_{j=1}^{N_t}\left(\frac{(1/N_z)\sum_{i=1}^{N_z}C_L(z_i,t_j)C_L(z_i-l_k,t_j)}{(1/N_z)\sum_{i=1}^{N_z}C_L^2(z_i,t_j)}\right)=\overline{\left(\frac{(1/N_z)\sum_{i=1}^{N_z}C_L(z_i,t_j)C_L(z_i-l_k,t_j)}{(1/N_z)\sum_{i=1}^{N_z}C_L^2(z_i,t_j)}\right)}^{t}, \tag{4}$$

where N_z is the total number of grid points along the spanwise direction and C_L is the lift coefficient. An identical definition is used for the drag coefficient autocorrelation function. For each length shift l_k, the autocorrelation function is computed by shifting the signal in order to obtain $C_L(z_i-l_k,t_j)$, multiplying it by the unshifted sequence $C_L(z_i,t_j)$, and then summing all the values of the product and normalizing. Here, the over-bar denotes a local averaging over time by means of a moving window of width N_t.

The signal $C_L(z_i,t_j)$ is taken to be the *fluctuation* of the original signal $C_L^*(z_i,t_j)$ from which we have subtracted its mean quantity (computed along a specific direction). This mean quantity can be computed along the spanwise direction for each time sample, or can be computed along the time–direction at each spanwise location. In the first case (Method 1), we have

$$C_L(z_i,t_j)=C_L^*(z_i,t_j)-\frac{1}{N_t}\sum_{n=1}^{N_t}C_L(z_i,t_n)=C_L^*(z_i,t_j)-\bar{C}_L^t(z_i), \tag{5}$$

while in the second case (Method 2), we have

$$C_L(z_i,t_j)=C_L^*(z_i,t_j)-\frac{1}{N_z}\sum_{m=1}^{N_z}C_L(z_m,t_j)=C_L^*(z_i,t_j)-\bar{C}_L^z(t_j). \tag{6}$$

These two methods provide very different results for standing wave force signals but similar results for traveling wave force signals. This has been verified with artificially built signals for validation purposes. Method 2 is very similar to the method used by Mansy et al. (1994), who were considering the three-dimensional structures associated with the secondary velocity flow. Their secondary flow was obtained by removing the two-dimensional primary flow from the original signal at each time. We prescribe the shift l_k to be

$$l_k=k\times l=k\times \mathrm{d}z \quad \text{with} \quad \mathrm{d}z=L/N_z \quad \text{and} \quad k=\left[0,1,2,\ldots,\frac{N_z}{2}\right]. \tag{7}$$

We have $N_z=64$ or $N_z=128$ points in the z-direction. The spatial spanwise periodicity of the quantity $C_L(z,t)$ is used to wrap up the signal in order to keep the same number of terms in the summation for all shifts. With this definition, the autocorrelation is symmetric around $l=0$, and it takes the value one for zero shift. In the present work, we use this autocorrelation function to compute the correlation length L_C of the hydrodynamic forces acting on the structure. In particular, we use different definitions to compute the correlation length. The first definition (Definition 1) corresponds to the first significant minimum of the autocorrelation profile given by Method 1. The second definition (Definition 2) is the crossing of the horizontal axis by the autocorrelation profile given by Method 2. The last definition (Definition 3) involves

$$L_C(t)=2\int_0^{\frac{L/D}{2}}R(l,t)\,\mathrm{d}l, \tag{8}$$

where $R(l,t)$ is the autocorrelation profile given by Method 1. This is done by numerically integrating the autocorrelation profile along the spanwise direction.

3. Response amplitude

We present amplitude response results for $\mathrm{Re}=1000$, 2000 and 3000. We investigate a total of seven different reduced velocities $V_{rn}=[3.76,4.18,4.62,4.99,6.0,7.0,8.0]$ for the oscillator, see Table 1. However, due to the cost of the computations at these Reynolds numbers, some of the cases corresponding to reduced velocities far away from the upper branch region ($V_{rn}=3.76$ and 8.00) were not investigated. Moreover, the case corresponding to $V_{rn}=4.62$ was only investigated for $\mathrm{Re}=1000$. In future work, it will be necessary to consider additional reduced velocities in order to obtain a better description of the shape of the upper branch (inverted U-shape or V-shape?). In the present work, the numerical values of the reduced velocities should be immediately adjacent (from below) or included in the region of poor correlation (Hover et al., 1998) or included in the lower branch response. The idea is to start from the region of

Table 1
Average one-tenth highest amplitude of response A_{max}/D versus nominal reduced velocity V_{rn} Reynolds number Re

	V_{rn}	Re = 1000	Re = 2000	Re = 3000
		A_{max}/D	A_{max}/D	A_{max}/D
Case I	3.76	0.60		
Case II	4.18	0.74	0.75	≈0.7*; 0.48
Case III	4.62	0.77		
Case IV	4.99	0.76	0.81	0.83*; 0.87
Case V	6.00	0.54	0.71	0.71
Case VI	7.00	0.55	0.54	0.55*
Case VII	8.00		0.54	

The asterisk indicates simulations performed with 128 points along the spanwise direction. Other simulations were performed using 64 points.

high correlation with $V_{rn} = 3.76$ and increase the value of V_{rn} toward $V_{rn} = 4.99$, referred as Case IV, and look for a drop in the spanwise correlation of the flow. Then, as we increase the reduced velocity toward the lower branch, we look for the recovery of larger correlation values. These nominal reduced velocities are defined based on the natural frequency f of the structure in vacuum. The reference reduced velocity $V_{rn} = V_{ref} = 4.18$, referred as Case II, was already investigated in Evangelinos (1999) but for a somewhat shorter cylinder ($L/D = 4\pi$).

Here, the average one-tenth highest amplitude is computed by first identifying the peak optimum values of the response signal. Then, the largest 10% values are kept and averaged over. For the case of Re = 1000, the response is noticeably larger for Cases II–IV. Surprisingly, the response remains large for Cases III and IV, even if the wake correlation coefficients present a sharp drop as seen in Lucor et al. (2003). Regarding the magnitude of the lift forces, we notice a decrease of the fluctuations of the *span-averaged* lift coefficient as we increase the reduced velocity. The time evolutions of the average lift force for Cases I and II are almost equivalent. However, the forces for Case III and particularly Case IV present a clear weakening and exhibit a beating phenomenon. The maximum instantaneous lift amplitude is obtained for Case II while the minimum for Case I.

The amplitude responses for Re = 2000 exhibit a general trend similar to the ones for Re = 1000. However, some noticeable differences are apparent. The upper branch resides higher and extends further to the right side. In particular, the response at $V_{rn} = 6.0$ is much larger. This clearly indicates a Reynolds number dependence of the location of the upper branch response.

Some of the simulations for Re = 3000 are carried out with different spanwise resolutions (see Table 1). An increase in the spanwise resolution does not seem to affect strongly the response except for Case II, where the response increased dramatically from 4.8 to a level close (see black star in Fig. 2) to the value for Re = 2000 at the same reduced velocity. In this case, the time integration of our simulation with high spanwise resolution was not long enough to produce accurate long-term statistics, but the trend is represented by the extrapolated dashed line as seen in Fig. 2.

Overall, these results are in good agreement with experimental results. For instance, the results for Re = 3000 compare well with the results by Hover et al. (1998).

4. Vortex synchronization patterns

As reported in Govardhan and Williamson (2000), there has been some debate concerning the vortex shedding modes that might be associated with the different response branches for the case of free transverse vibrations. While the 2S vortex formation mode associated with the initial branch is well documented for 2D and 3D computations (Meneghini and Bearman, 1995; Blackburn and Henderson, 1999; Evangelinos, 1999; Evangelinos and Karniadakis, 1999), the 2P vortex mode associated with the upper and lower branches is rarely reported in numerical works (Blackburn et al., 2000). In particular, to our knowledge, there does not exist a clear numerical result that establishes the existence of the 2P vortex mode as a steady state pattern for any low mass-damping response of a long rigid cylinder outside the initial branch region. To this end, we perform flow visualizations of the near-wake and frequency response for cases with reduced velocity outside of the initial branch. More specifically, we investigate the existence of a Reynolds number effect [as proposed by Govardhan and Williamson (2000)], that would explain the discrepancy between

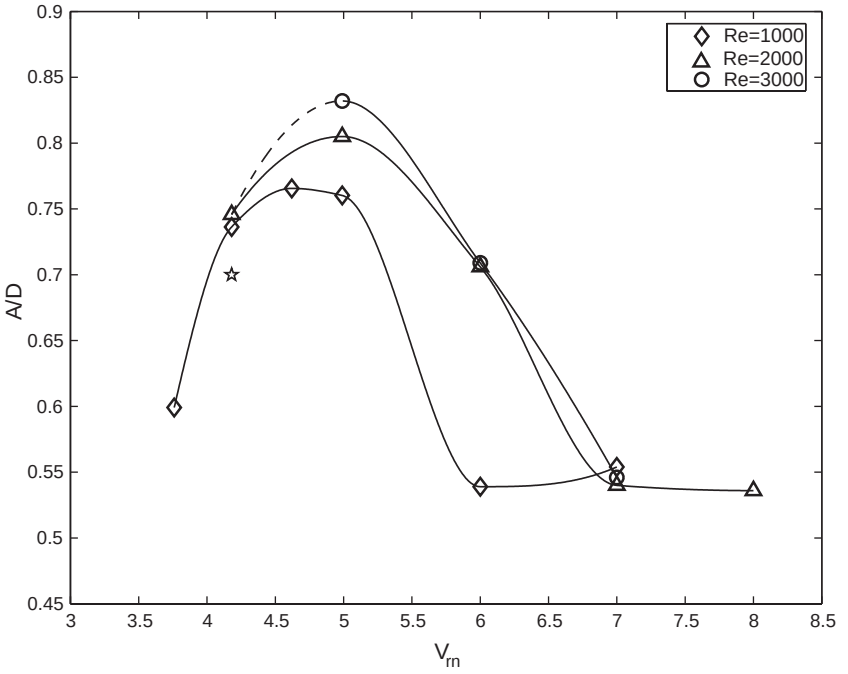

Fig. 2. Average one-tenth highest amplitude response $A_{\max}/D$ as a function of reduced velocity V_{rn} for different Re. The black star corresponds to the nonfully converged simulation with 128 points along the span at $\mathrm{Re} = 3000$ and $V_{rn} = 4.18$.

experimental and numerical results. We present flow visualizations and frequency response results for $\mathrm{Re} = 1000$, 2000 and 3000.

4.1. Flow visualizations

Flow visualizations are very useful, even for flows past rigidly moving cylinders where one would expect strongly correlated wake vortical structures aligned with the cylinder axis. However, this is not always the case, as seen in Fig. 3, when the reduced velocity corresponds to a transition region between two possible wake states. Figs. 4–6 show phase (over 3 cycles) and span-averaged isocontours of the pressure and spanwise vorticity fields in the near-wake of the cylinder. It is worth mentioning that these isocontours are not accurate and representative of the flow features in the immediate vicinity of the cylinder for $|r| = [(x/D)^2 + (y/D)^2]^{1/2} \leqslant 1$. This is due to the post-processing isocontour routine. Moreover, each three-dimensional spanwise vorticity field has been gently filtered, using a three-dimensional convolution filter, in order to remove the smaller weak structures resulting from the intermittent small scale three dimensionality of the flow. For Figs. 4 and 5, each plot is separated by a $\frac{1}{4}$ period. Top and bottom left images show the cylinder wake when the body is at the bottom or top of its stroke, respectively. Top and bottom right images show the wake when the cylinder is at the center of its lateral oscillation and the body is moving up or down, respectively. Fig. 6 captures two different locations of the body motion that are separated by $\frac{1}{2}$ a period. These two locations do not represent the extrema of the cylinder motion.

Before describing and analyzing the images, it is crucial to point out the limitations of the averaging process that we use in our simulations. Flow visualizations from experimental works usually present views of the wake at some cylinder (top and median) extreme positions. In our computations, the actual implementation requires each flow field to be saved at regular time intervals. The required sampling frequency in the case of a free motion is difficult to predict a priori. Ideally, if the free cylinder response is purely harmonic with frequency of oscillation f_s, the sampling frequency can be taken to be equal to a multiple of f_s. In our case, we use the natural frequency f_n of the body. As we will see later, those two frequencies are distinct in most cases. Therefore, the difference prohibits long time averaging as the different frames over which we phase-average shift in space. Obviously, averaging over three cycles is not enough to obtain explicit visualizations [10 cycles would be more appropriate (Govardhan and Williamson, 2000)]. We estimate that there is a 10% error in the averaged location of the cylinder in Figs. 4–6. It should be mentioned that the time scale associated

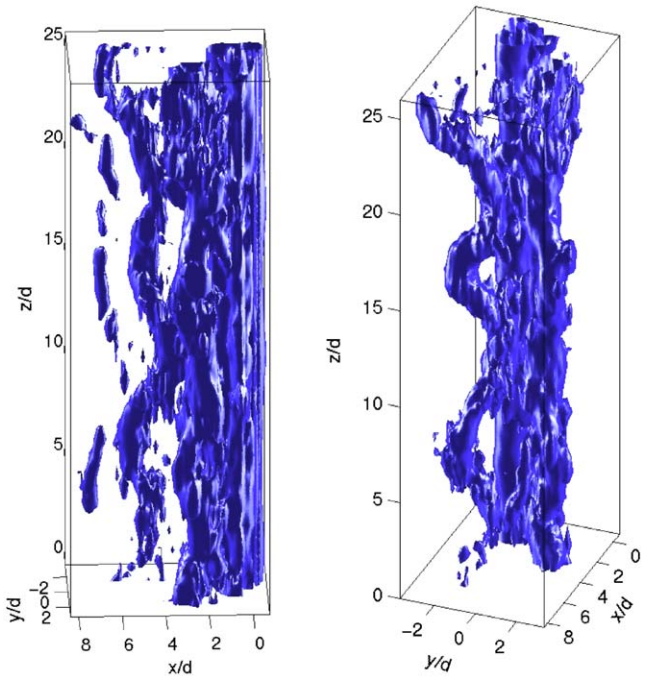

Fig. 3. Two different isocontour views of the same instantaneous pressure in the near-wake of a moving rigid cylinder subject to VIV at Re = 3000 (Case IV: $V_m = 4.99$). Left plot: flow from right to left; Right plot: downstream view, almost parallel to the plane of the inflow.

with the vortex shedding is much larger than the sampling scale so that the Nyquist criterion is not violated.[1] Another factor which affects the clarity of the results is the three dimensionality of the wake combined with the span averaging. Span-averaged values of strongly three-dimensional flow structures (see Fig. 3) get smeared and can mask the presence of the 2P vortex shedding. This is particularly true for the middle-range wake ($8 \leqslant x/D \leqslant 13$ in our pictures) where inherent three dimensionality takes place.

From Figs. 4–6, it is clear that we observe a 2P vortex shedding (that two pairs of vortices formed per cycle). As the cylinder reaches its lowest position (Fig. 5, top-left image), the lower anti-clockwise vorticity structure created by the lower shear layer starts stretching and is finally pinched off and to split into two parts. As the cylinder moves up, the upper part forms a weaker anti-clockwise light vortex beside the stronger clockwise dark vortex (Fig. 5, top-right image). These two vortices form a pair. The same mechanism takes place on the other side as the cylinder reaches its highest position and then moves down (Fig. 5, bottom-left and right images). The deformation, stretching and splitting of the main vorticity as described by Govardhan and Williamson (2000) has been clearly observed by looking at movies based on our simulation of the wake at Re = 1000 for instance. The strength of the second vortex of each pair is much weaker than the first vortex and remains somewhat attached to the vortex of the opposite sign shed next. The weaker circulation strength of the second vortex has also been documented by Govardhan and Williamson (2000). As we look downstream, it is sometimes difficult to clearly identify the location of the second vortex as it weakens along the streamwise direction, see Fig. 7. We have circled the locations of the vortices for the case of Re = 2000 on the two-dimensional plot of Fig. 6. Fig. 7 shows isosurfaces of phase-averaged (over three cycles) filtered spanwise vorticity field corresponding to the same situation as the top-right image of Fig. 6. Next, we pursue our quest for the *existence* and *persistence* of the 2P vortex shedding in the lower branch region by looking at the frequency response of the structure and the wake.

[1]One of the referees proposed a simple solution to this problem, which is to monitor the response of the structure during the computation and to use it as a sampling trigger. This is a good idea for rigid motions. In the case where we would be interested in sampling the flow at some optimal displacements that might change in time, monitoring of the cylinder velocity and acceleration would help as well. Unfortunately, it was not implemented at the time we performed the computations.

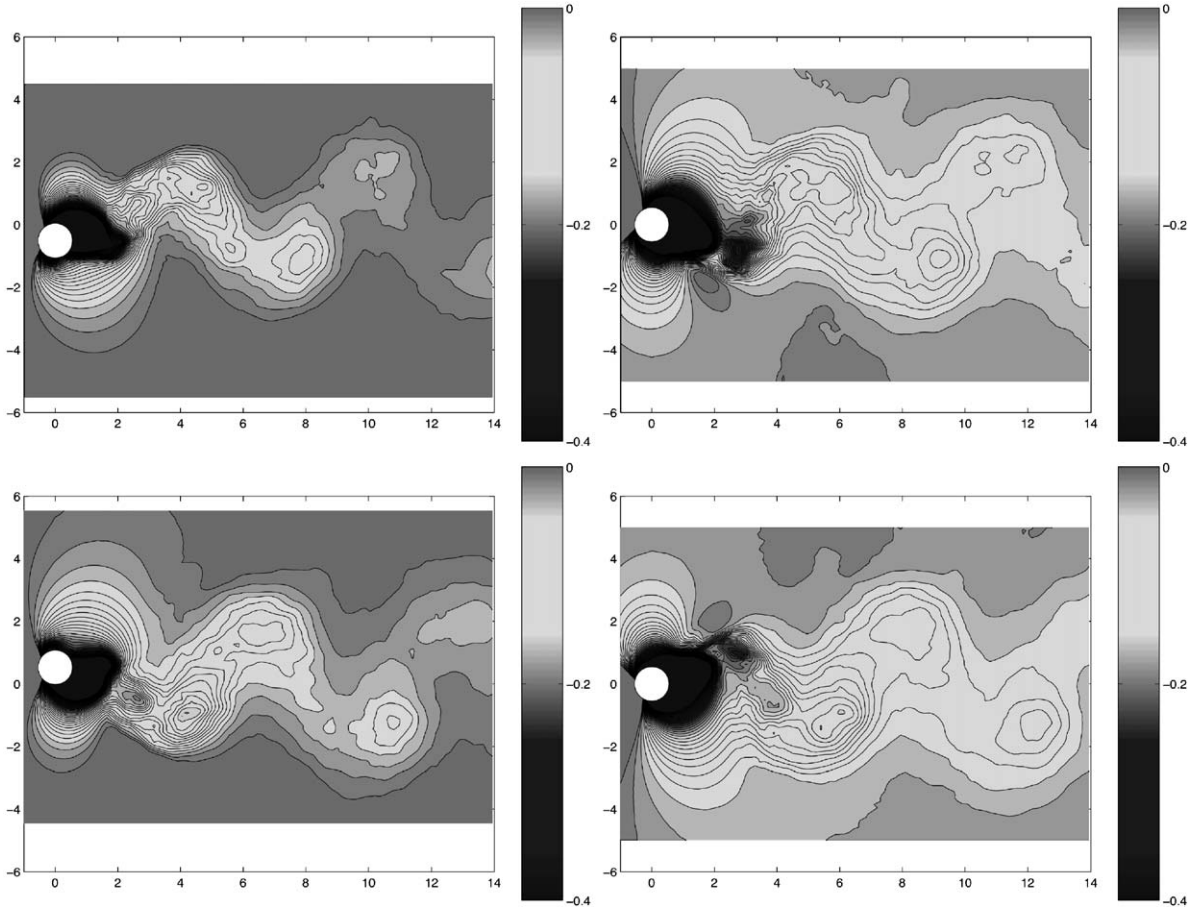

Fig. 4. Isocontours of span and phase-averaged pressure field in the near-wake of a moving rigid cylinder at $V_{rn} = 7.0$, $\mathrm{Re} = 1000$ and $A_{\max}/D = 0.55$. Upper-left: cylinder bottom extreme position; Upper-right: cylinder median position, moving upward; Lower-left: cylinder top extreme position; Lower-right: cylinder median position, moving downward.

4.2. Frequency response

The classic *lock-in* phenomenon known as a synchronization of the vortex shedding frequency f_v and the cylinder oscillation frequency f_s with the natural frequency f_n of the body induces a ratio f_s/f_n close to one over some range of reduced velocity V_{rn}. This is particularly true for large to moderate mass ratios but does not hold well for low mass ratios. Instead, Khalak and Williamson (1999) suggest another definition of the synchronization as a ratio f_v/f_s close to one, which implies that the fluid force-frequency must match the shedding frequency. Moreover, the range or synchronization regime over which lock-in happens widens in the case of low mass ratios.

Fig. 8 shows the structural frequency response, which we have taken to be the ratio between the frequency of oscillation f_s and the natural frequency f_n of the body, for three different Reynolds numbers. We see that we obtain, approximately, the same response for all three Reynolds numbers. The response for $V_{rn} = 4.18$ and $\mathrm{Re} = 3000$ stands out as it corresponds to the case with insufficient spanwise resolution, see Table 1. The agreement between the different cases is very good for reduced velocities $V_{rn} \leqslant 6$. In this case, the response grows almost linearly and the ratio reaches a value close to unity for $V_{rn} \approx 6$ for all Reynolds numbers. This corresponds to the jump in total phase as the frequency of oscillation f_s passes through the natural frequency in vaccum f_n (Govardhan and Williamson, 2000). For higher reduced velocities the response remains almost constant for all cases except for a lower value at $\mathrm{Re} = 1000$. These results are in good quantitative agreement with the results of Hover et al. (1998) (see crosses) at a somewhat higher $\mathrm{Re} = 3800$. Here, each cross is an averaged value over their duplicate or triplicate tests at the same reduced velocity.

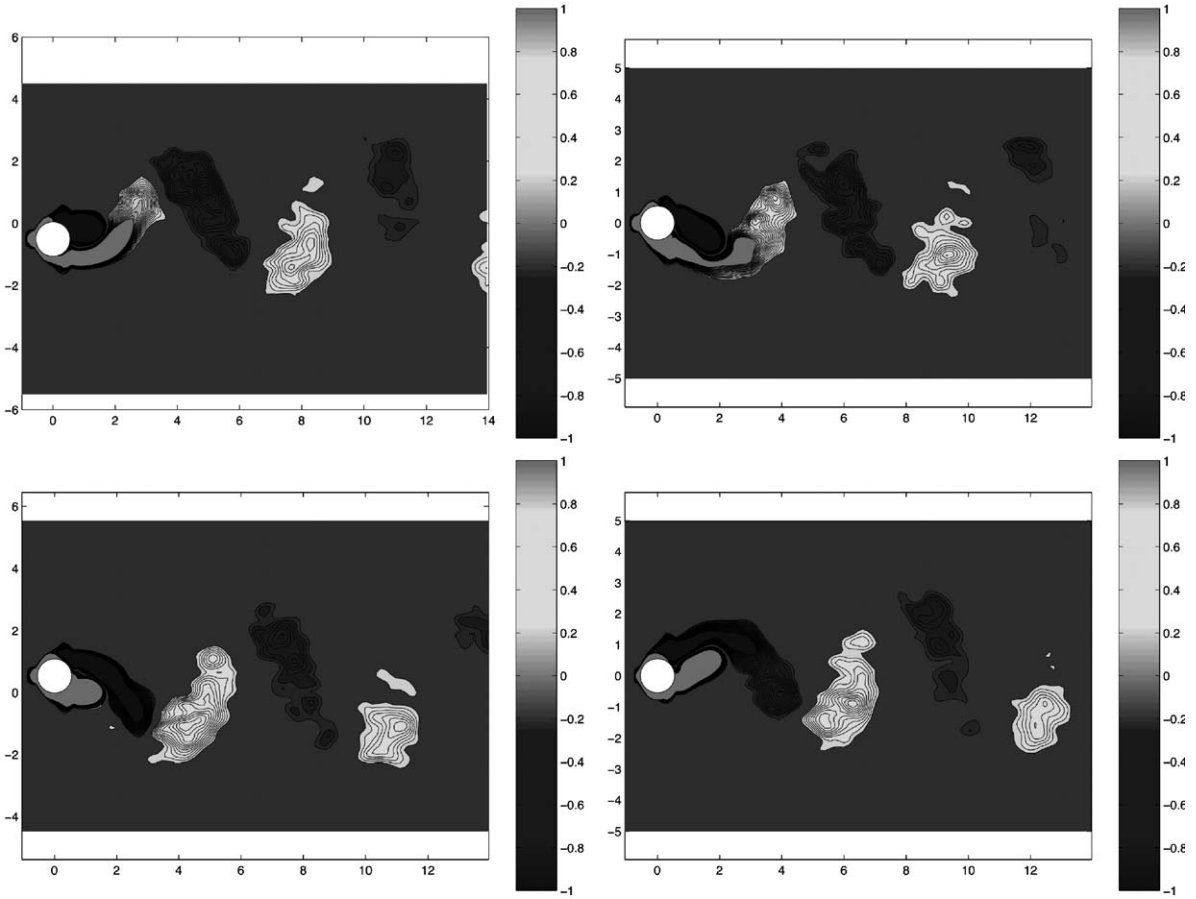

Fig. 5. Isocontours of span and phase-averaged pressure field in the near-wake of a moving rigid cylinder at $V_{rn} = 7.0$, $\mathrm{Re} = 1000$ and $A_{\max}/D = 0.55$. Upper-left: cylinder bottom extreme position; Upper-right: cylinder median position, moving upward; Lower-left: cylinder top extreme position; Lower-right: cylinder median position, moving downward.

Figs. 9 and 10 present the shedding frequency spectra f_v normalized with the natural frequency f_n of the cylinder, for $\mathrm{Re} = 1000$ and $\mathrm{Re} = 2000$, respectively. The frequency f_v is the frequency of the cross-flow velocity in the wake and is measured at six different locations in the near-wake of the cylinder. The cross-flow velocity component is sampled at these points for a long time integration and we compute its spectrum to obtain the shedding frequency. The coordinates of the six points are: $A(x/D = 1, y/D = 0)$; $B(x/D = 1, y/D = 1)$; $C(x/D = 3, y/D = 0)$; $D(x/D = 3, y/D = 1)$; $E(x/D = 5, y/D = 0)$; $F(x/D = 5, y/D = 1)$. Unfortunately, no history points were placed at locations corresponding to negative values of y/D. This was based on the assumption of symmetry of the wake which might not be valid in the case of a P + S vortex shedding.

Both cases illustrate the importance of the choice of these points. For both Reynolds numbers, we see that the shedding frequency response for points placed along the $y = 0$ axis at a reasonable distance away from the body, peaks at a single frequency where the ratio is close to unity. These results do not imply a 2P shedding mode but instead a 2S shedding mode, where only one pair of vortices is shed per cycle. However, points placed along the $y = 1$ axis, away from the axis of symmetry of the body, also clearly exhibit a peak at twice the frequency and the ratio is in this case close to two. This indicates two pairs of vortices shed per cycle which is the trademark of a 2P shedding mode. A careful examination of the data confirms this analysis. The strength of the second peak relative to the first one for point B for instance is close to 100% for $\mathrm{Re} = 1000$ and $\mathrm{Re} = 2000$, and for point D, it is close to 25% for $\mathrm{Re} = 1000$ and 20% for $\mathrm{Re} = 2000$ and it becomes lower for point F. These results exclude harmonic numerical effects misinterpretation. It seems that the center locations of the two vortices shed per half-cycle do not remain aligned with the $y = 0$ axis as they move downstream. This can be seen in Fig. 6, where the center of one of the vortices of each pair, for points located three and five diameters downstream, respectively, lie closer to the $y = 1$ axis than the $y = 0$ axis. This would explain

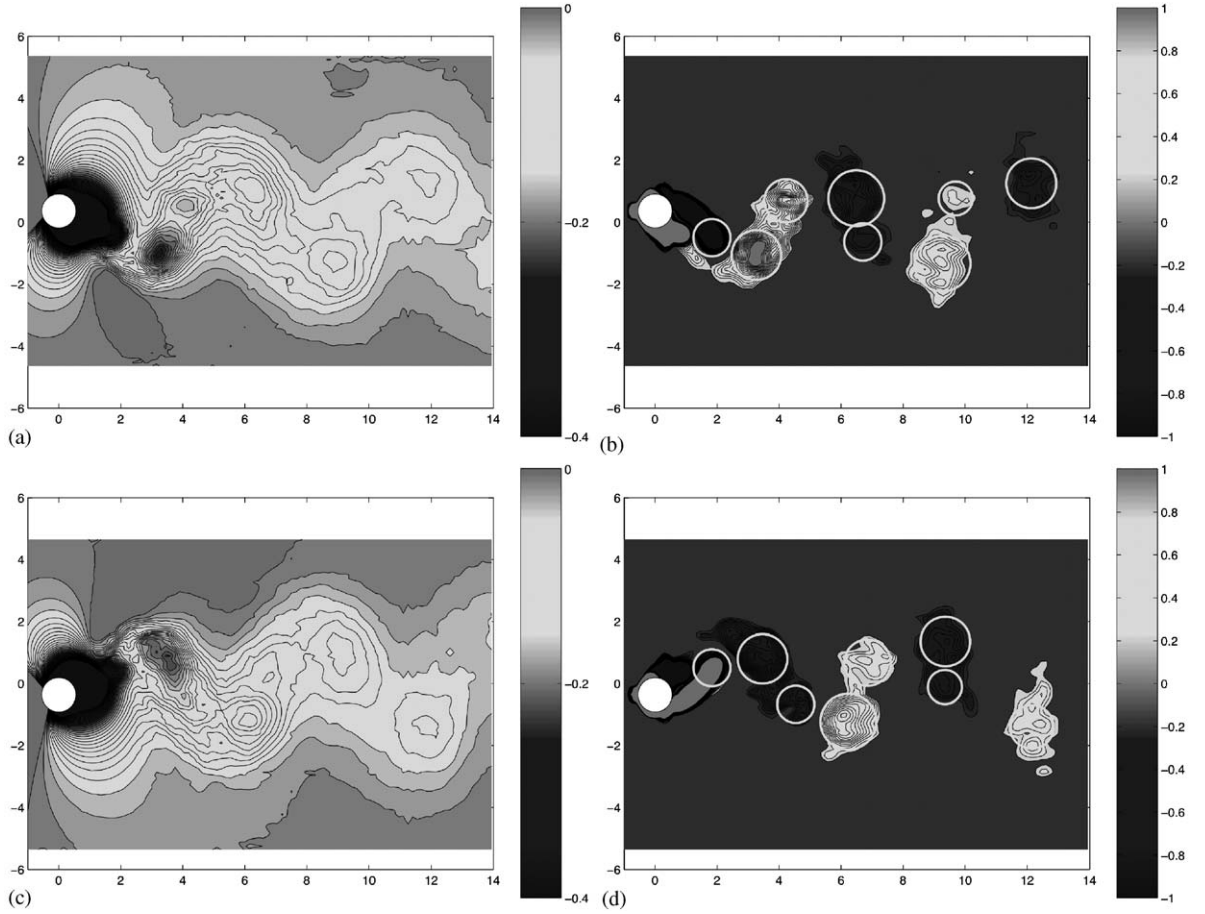

Fig. 6. Isocontours of span- and phase-averaged pressure and spanwise vorticity fields in the near wake of a moving rigid cylinder at $V_{rn} = 7.0$, $\mathrm{Re} = 2000$ and $A_{\max}/D = 0.54$. 2P vortices have been circled. (a) Cylinder bottom extreme position; (b) cylinder median position, moving upward; (c) cylinder top extreme position; (d) cylinder median position, moving downward.

why the second vortex is not captured by the history points lying on this axis. The two points placed very close to the cylinder give a peak close to one as well as other harmonics. In particular, the point located in the upper shear layer $(x/D = 1, y/D = 1)$ provides multiple harmonics with decaying power. It holds as much power in the main frequency as in the first harmonic.

Based on these studies it seems reasonable to say that we have obtained a stable periodic 2P vortex wake mode with formation of two same-sign vortices within each half-cycle. The strength of the second vortex of each pair is weaker than the first vortex. Moreover, it is rather difficult to clearly identify the 2P mode in the wake as three dimensionality of the vortical structures develops along the spanwise direction as they travel downstream.

5. Phasing analysis

5.1. Complex demodulation

We present numerical results for $\mathrm{Re} = 1000$, 2000, 3000 and focus on the reduced velocities $V_{rn} = [4.99, 6.0]$. These values should be immediately adjacent (from below) or included in the region of poor correlation or included in the lower branch response. These nominal reduced velocities are defined based on the natural frequency f of the structure in vacuum. Figs. 11–16 present *complex demodulation* results for the cylinder displacement and lift force signals. For each

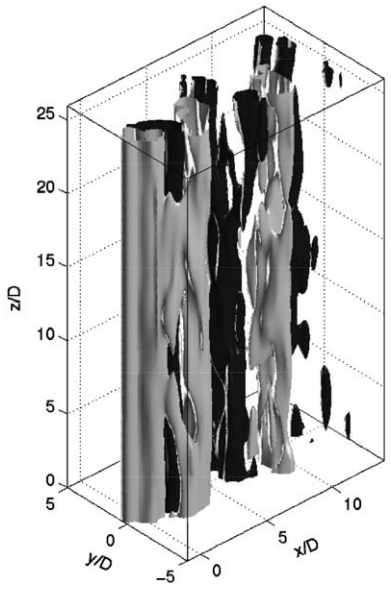

Fig. 7. Isosurfaces of phase-averaged filtered spanwise vorticity fields in the near-wake of a moving rigid cylinder at $V_{rn} = 7.0$, $\mathrm{Re} = 2000$ and $A_{\max}/D = 0.54$. Vortex pairs of the 2P mode are easier to spot at some locations along the span than others. For instance, the 2P mode is very clear in the upper third region of the wake.

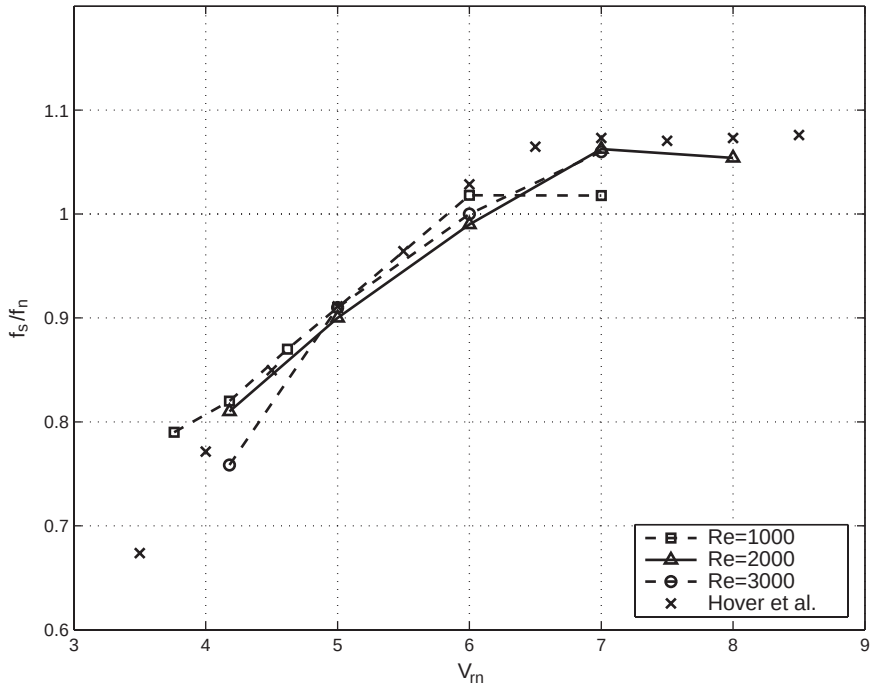

Fig. 8. Structural frequency response f_s/f_n as a function of reduced velocity V_{rn} for different Reynolds numbers. The crosses correspond to experimental results by Hover et al. (1998).

case, we show the spatio-temporal evolutions of the lift coefficient C_L, the amplitude of the demodulated lift coefficient R_{C_L} and the phase difference $\Delta\Phi$ between the demodulated cross-flow displacement and the demodulated lift coefficient. The horizontal axis represents nondimensional time and the vertical axis represent the nondimensional

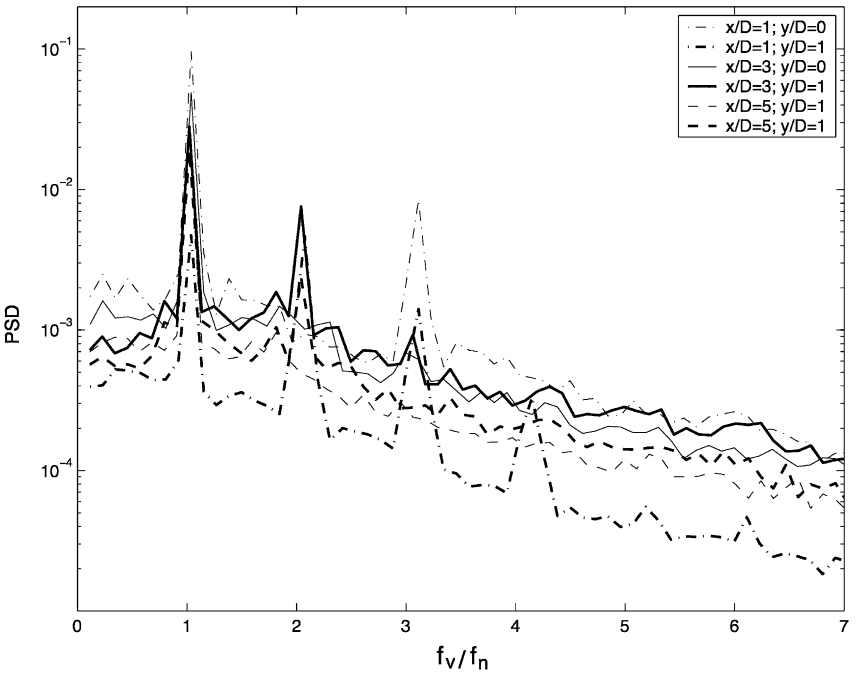

Fig. 9. Shedding frequency response f_v/f_n for Re = 1000 with $V_{rn} = 7.0$ (Case VI) at six different locations in the wake (see legend).

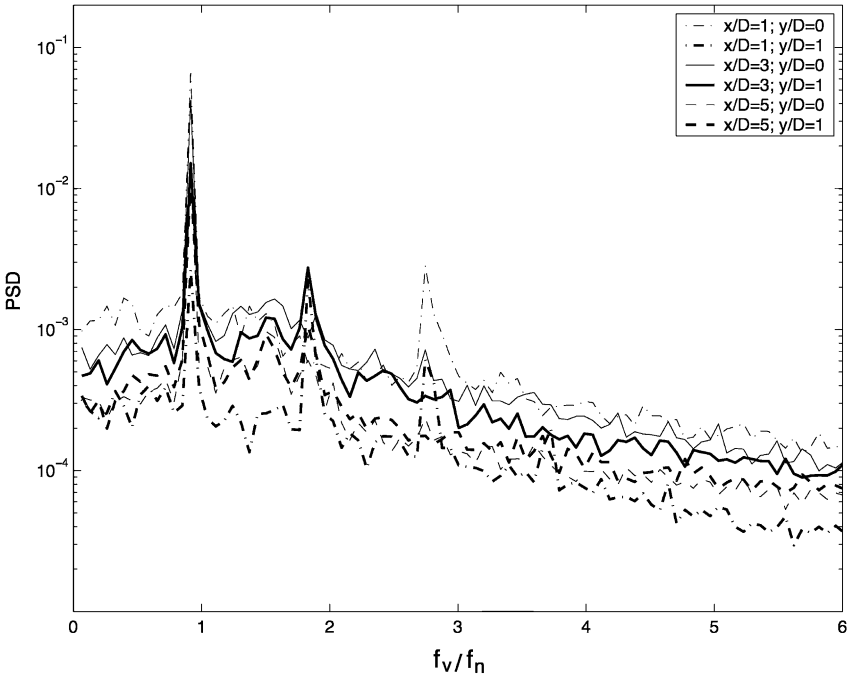

Fig. 10. Shedding frequency response f_v/f_n for Re = 2000 with $V_{rn} = 7.0$ (Case VI) at six different locations in the wake (see legend).

spanwise direction. For each case, the demodulation frequency is chosen to be the leading oscillation frequency of the structure. The width of the temporal window of the filter varies from case to case from one-fifth to one-tenth of one oscillation period.

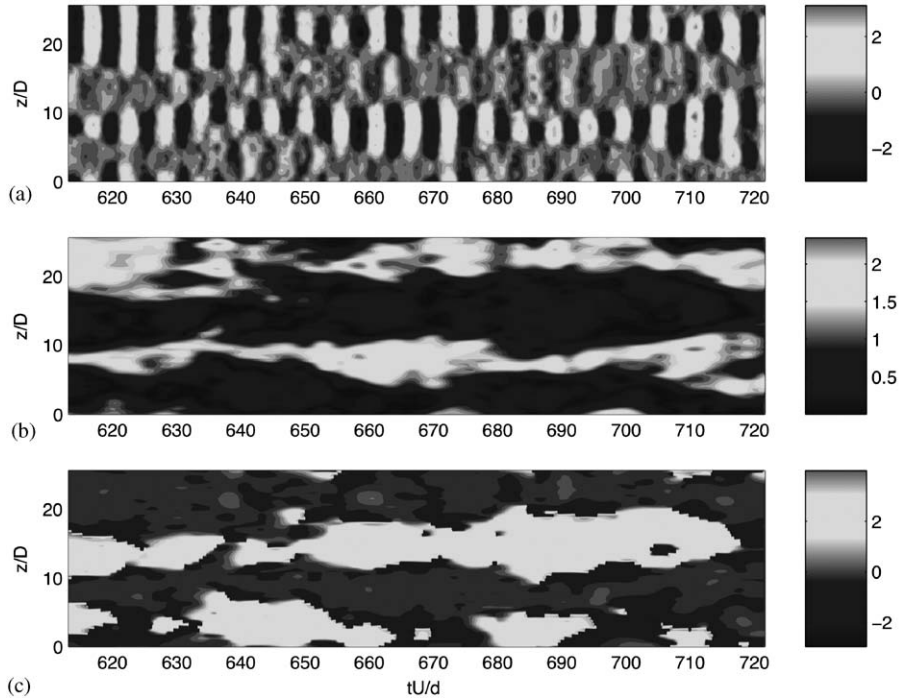

Fig. 11. Complex demodulation analysis for $\mathrm{Re} = 1000$ and $V_{rn} = 4.99$. (a) Isocontours of Lift coefficient C_L. (b) Isocontours of amplitude of demodulated Lift coefficient R_{C_L}. (c) Isocontours of phase difference $\Delta\Phi$ between demodulated cross-flow displacement and demodulated lift coefficient.

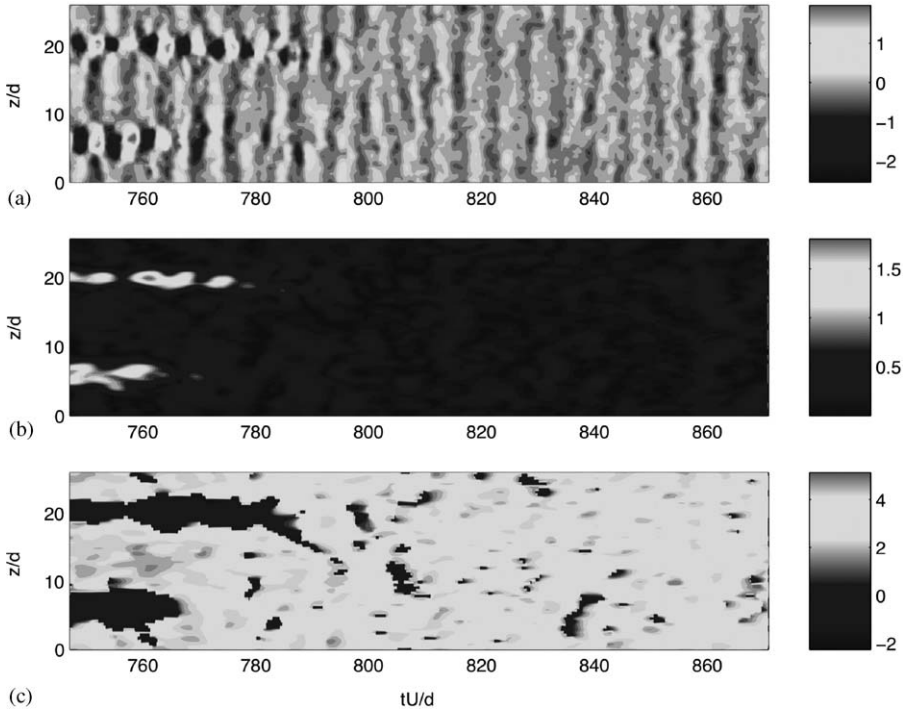

Fig. 12. Complex demodulation analysis for $\mathrm{Re} = 1000$ and $V_{rn} = 6.00$. Same legend as in Fig. 11.

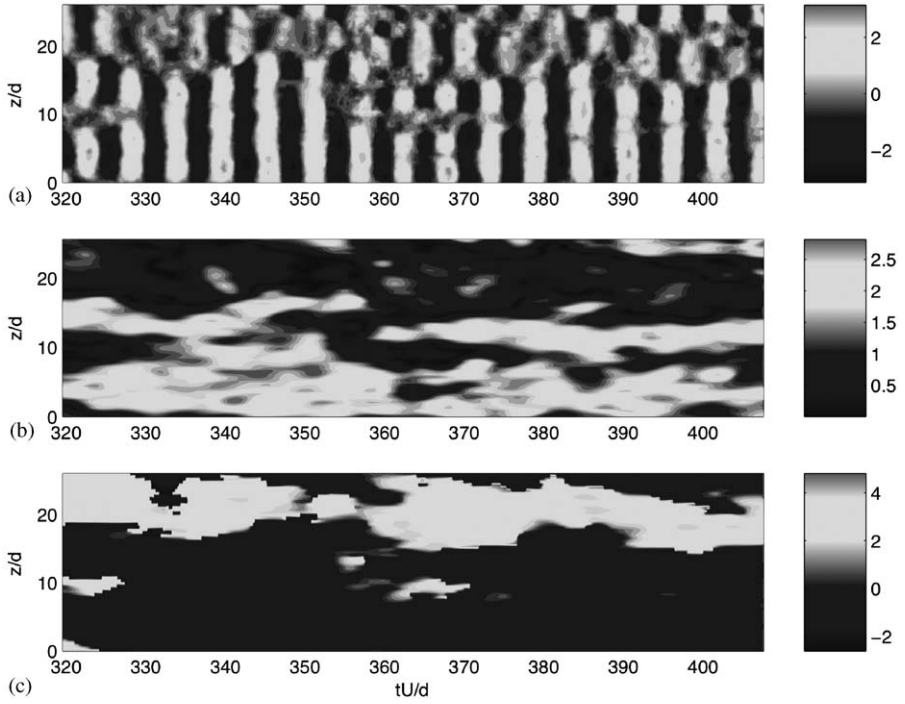

Fig. 13. Complex demodulation analysis Re = 2000 and $V_{rn} = 6.00$. Same legend as in Fig. 11.

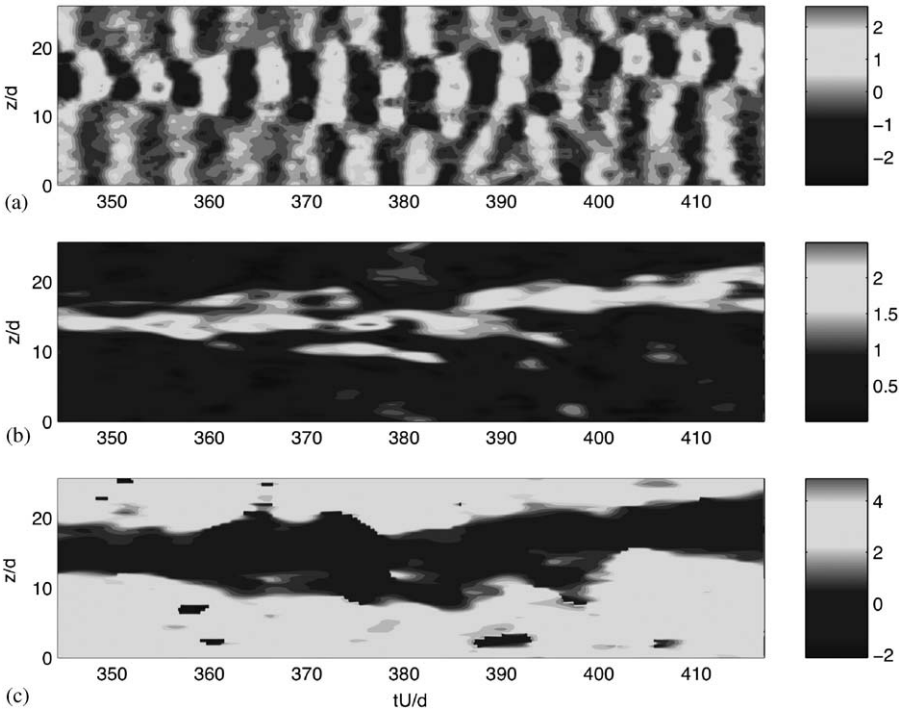

Fig. 14. Complex demodulation analysis for Re = 2000 and $V_{rn} = 6.00$. Same legend as in Fig. 11.

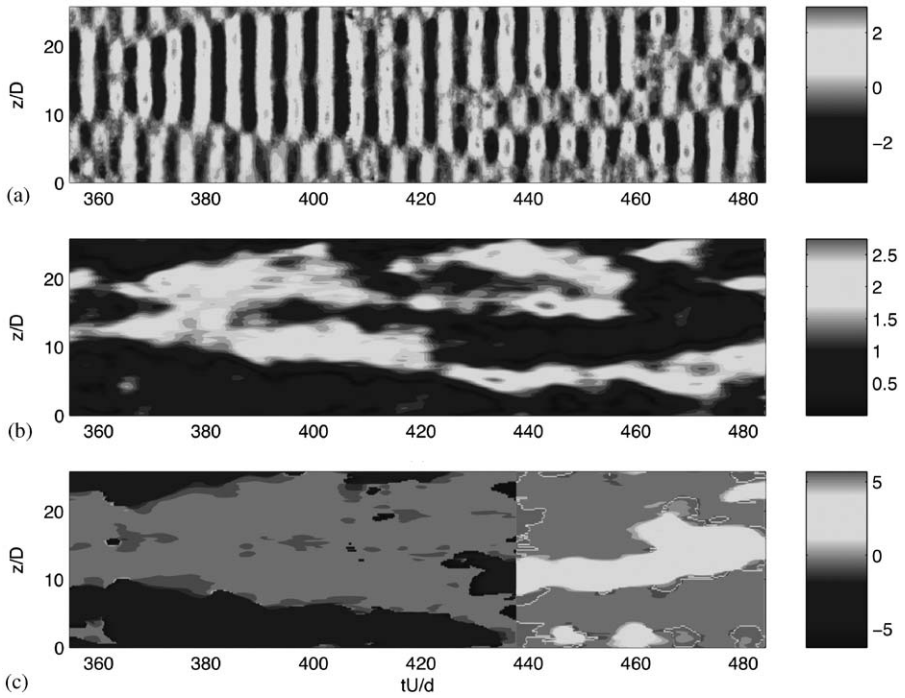

Fig. 15. Complex demodulation analysis for Re = 3000 and $V_{rn} = 4.99$. Same legend as in Fig. 11. (The sharp discontinuity is due to the wrapping of the phase and does not have a significant physical meaning.)

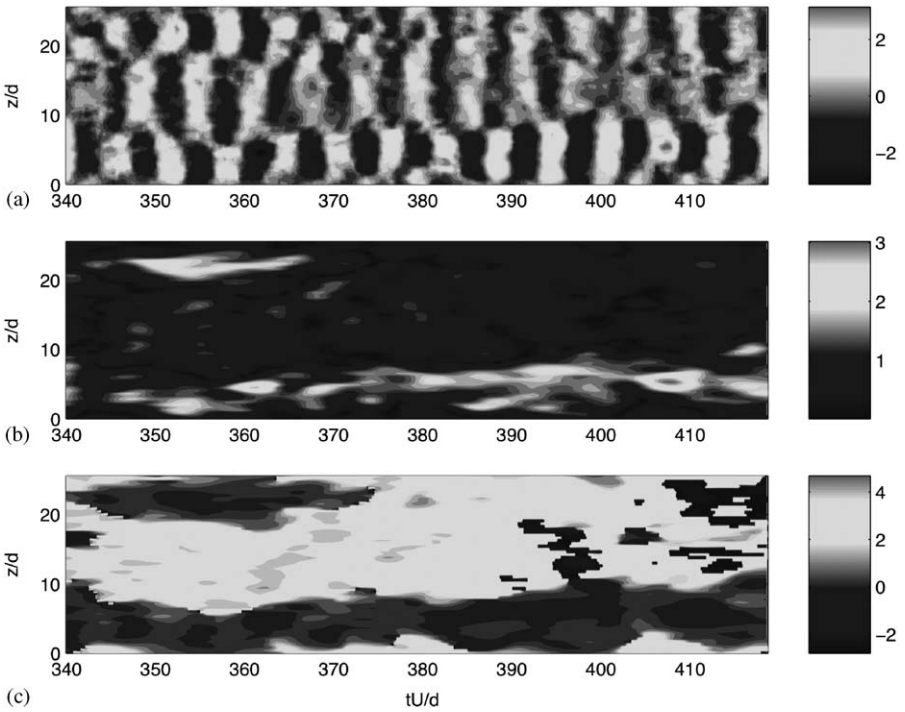

Fig. 16. Complex demodulation analysis for Re = 3000 and $V_{rn} = 6.00$. Same legend as in Fig. 11.

In most cases, for these chosen reduced velocities, we see that the three dimensionality of the flow is well developed. Consequently, the forces are poorly organized along the span. The maximum lift coefficient is subject to large modulation. The correspondence between the plots is striking as the method isolates alternating streak regions (see Figs. 11(b) and 13–16(b)) of small and large amplitude of demodulated lift that clearly correspond to regions of small and large forcings (see Figs. 11(a) and 13–16(a)). Finally, Figs. 11–16(c) show the phase difference (in radians mod 2π) between the two demodulated signals (lift and displacement). Again, regions of high lift amplitude forces correspond to regions where the cylinder displacement and lift forces are in phase, i.e. $\Delta\Phi(t,z) \approx 0$. More interestingly, regions of low lift amplitude forces correspond to regions where the cylinder displacement and lift forces are out of phase, i.e. $\Delta\Phi(t,z) \approx \pi$, which explains the overall drop of spanwise correlation. Indeed, strong three dimensionality in the wake induces forces on the cylinder with poor correlation. In this case, the net excitation force becomes smaller.

Fig. 12 shows the case corresponding to the reduced velocity $V_{rn} = 6.00$ at $\mathrm{Re} = 1000$. It is noticeably different from the cases with the same reduced velocity at $\mathrm{Re} = 2000$ (see Fig. 14) and at $\mathrm{Re} = 3000$ (see Fig. 16). In that case, after an initial transient, the streaks disappear and a more uniform state appears with low forces and a phase difference close to π. This is characteristic of the lower branch response with a 2P shedding mode (Lucor, 2004). These results indicate a Reynolds number effect in the location of the region of poor correlation. The transition between the upper and lower branches could be delayed to higher reduced velocities in the case of higher Reynolds numbers.

Figs. 11–16 clearly demonstrate that in this region of transition with poor correlation, the wake does not switch intermittently from one mode with a good phasing ($\Delta\Phi \approx 0$) to another mode with a poor phasing ($\Delta\Phi \approx \pi$) across the entire span. It also shows that it does not transition progressively and continuously with increasing reduced velocity, by passing through the entire range of phase angles from 0 to π. Instead, there exist two unique phase angle values of 0 and π that coexist along the span. As we have seen previously, they form alternating streaky regions extending along the span. The time evolution of the locations as well as the relative dominance of these regions as a function of Reynolds numbers and reduced velocities are very important. Fig. 17 shows the time traces of the span-averaged value of the phase difference between structural motion and lift coefficient. At any given time, a value close to 0 would indicate a very good phasing across the entire span and a value close to π would indicate the opposite. A value of $\pi/2$ might indicate that both states are equally represented. We notice that the mean phase difference is closer to π for $V_{rn} = 6.00$.

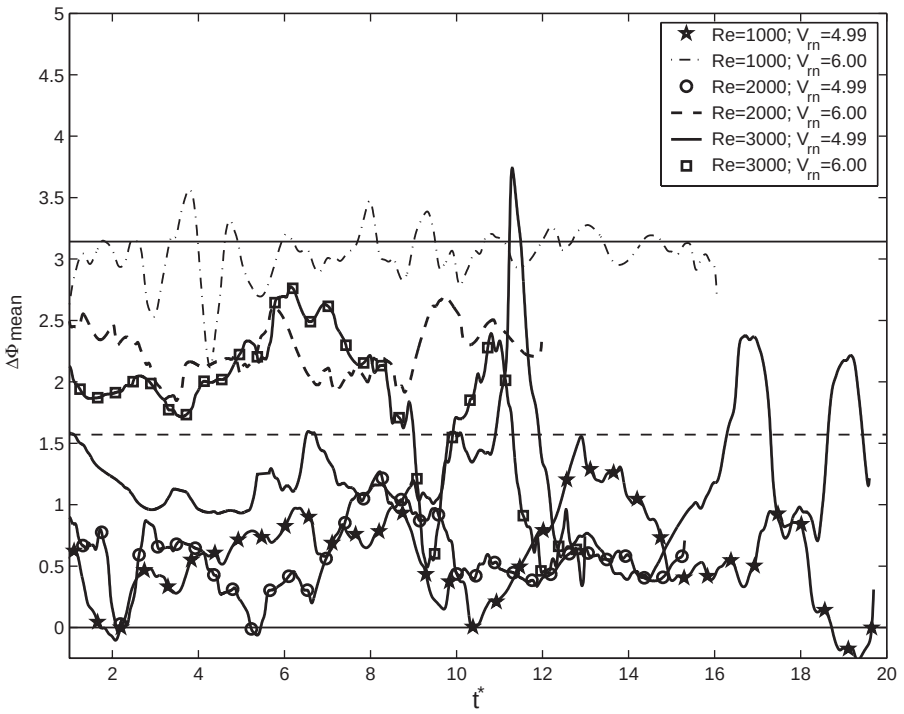

Fig. 17. Time traces of span-averaged phase difference $\Delta\Phi$. The horizontal black lines (solid top line, middle dashed line and bottom solid line) indicate a span-averaged phase difference $\Delta\Phi$ of π; $\pi/2$; and 0, respectively (the absolute value of the phase difference for $\mathrm{Re} = 3000$ and $V_{rn} = 5.99$ is used to avoid a sharp discontinuity).

This indicates that this reduced velocity is closer to the region of lower branch response. This is particularly true for $\mathrm{Re} = 1000$. At this reduced velocity, results for $\mathrm{Re} = 3000$ exhibit stronger modulation in time than $\mathrm{Re} = 2000$ results. Mean phase differences for $V_{rn} = 4.99$ show large modulation in time and can oscillate from a state where the phase difference is close to zero to a state with an averaged phase difference close to $\pi/2$. At this reduced velocity, results for $\mathrm{Re} = 3000$ show an averaged phase difference that is closer to $\pi/2$ than the $\mathrm{Re} = 1000-2000$ results. However, this signal exhibits large deviations from the mean.

We should also mention that the jump of π in the total phase (phase between the total lift force and the cylinder motion), between the upper and lower branch for cases away from the transition region was successfully captured (Lucor, 2004). Complex demodulation analysis and phase-plane plots of displacement versus lift for $\mathrm{Re} = 1000-2000$ produced a clear π phasing between the two signals, as expected from experimental work (Govardhan and Williamson, 2000).

5.2. Correlation length

Here, we summarize the correlation length results for the three Reynolds numbers and at each reduced velocity using the methods and definitions described in Section 2.2. Each presented correlation length is a nondimensional quantity. These results should be compared with the results of Fig. 2.

Fig. 18 shows the correlation length results for the drag and lift force coefficients. These results are obtained by treating signals according to Method 1, see Section 2.2. Once the autocorrelation profiles are obtained for each Reynolds number and reduced velocity, the functions are integrated according to Definition 3. Both drag and lift results look qualitatively similar and take the form of an inverted bell. The correlation lengths are very large for low reduced velocities around $V_{rn} = 4$ corresponding to the initial branch or the left of the upper branch (see Fig. 2). Then there is a drop in the correlation for intermediate reduced velocities between $V_{rn} = 5$ and $V_{rn} = 6$ close to the transition region. Finally, the correlation increases for larger reduced velocities corresponding to the lower branch of response. Nevertheless, there exist a clear difference between the $\mathrm{Re} = 1000$ and the $\mathrm{Re} = 2000-3000$ results. In the $\mathrm{Re} = 1000$ case, the loss of correlation occurs over a narrower region and takes place at lower reduced velocity. In particular, the difference is very large between the two groups for $V_{rn} = 6$. It is worth mentioning that in this case the autocorrelation profiles for $\mathrm{Re} = 2000$ and $\mathrm{Re} = 3000$ both exhibit negative values for large shifts. This explains the small integrated values of the corresponding correlation lengths. However, the profiles for these cases do not take an oscillatory shape typical of travelling wave responses (Mansy et al., 1994). This suggest that the flow in these cases remains somewhat organized along the spanwise direction, (e.g. Figs. 14 and 16). The solid black diamond and pentagon markers show the correlation lengths when we consider the absolute value of the autocorrelation profiles in Definition 3 instead.

This approach (Method 1 and Definition 3) is not sufficient to give a good description of the system. For instance, the lift correlation length results for $V_{rn} = 7.0$ are significantly lower than the ones for $V_{rn} = 6.0$. However, a careful examination of the force distribution along the span reveals a well organized flow field in both cases. The difference resides in the magnitude of the forces. The handicap of this approach can be illustrated by the case where one builds two different signals with same spanwise fluctuations but different spanwise means. In this case, the computed correlation lengths are different when using Method 1 and Definition 3. However, the use of Method 2 combined with Definition 2 does produce the same correlation lengths.

Fig. 19 shows the correlation length results for the drag and lift force coefficients. These results are obtained by treating signals according to Method 2. Once, the autocorrelation functions are obtained for each Reynolds number and reduced velocity, we compute the shift at which the profile crosses the $y = 0$ axis (Definition 2). This corresponds to the typical length over which the force *fluctuation* keeps the same sign. Both drag and lift results look qualitatively similar with lengths approximately constant ($V_{rn} = 6.0$ and $V_{rn} = 7.0$ giving similar results this time) for all reduced velocities and Reynolds numbers except for $\mathrm{Re} = 2000-3000$ for reduced velocities around $V_{rn} = 6$. For this reduced velocity, the force fluctuations are larger and more organized along the span.

Generally, if the cylinder is long compared to the typical length over which the correlation coefficients remain large, not all vortices cause forces in phase with each other, and the net excitation force is smaller. Time averaging is also another issue for signals that exhibit strong beating in time. Some important features could be masked by the time averaging. In the following, we show results where we perform a local time averaging by using a moving window of width $N_t = 15$ time units, which corresponds approximately to three shedding periods. Fig. 20 shows the time evolution of the correlation lengths of the lift coefficient for each case. The time axis t^* is properly scaled for each case with the corresponding leading oscillation frequency so that it has units of shedding cycles. Overall, the forces are not well correlated with maximum values slightly larger than half the span. The correlation lengths are very small (of the order

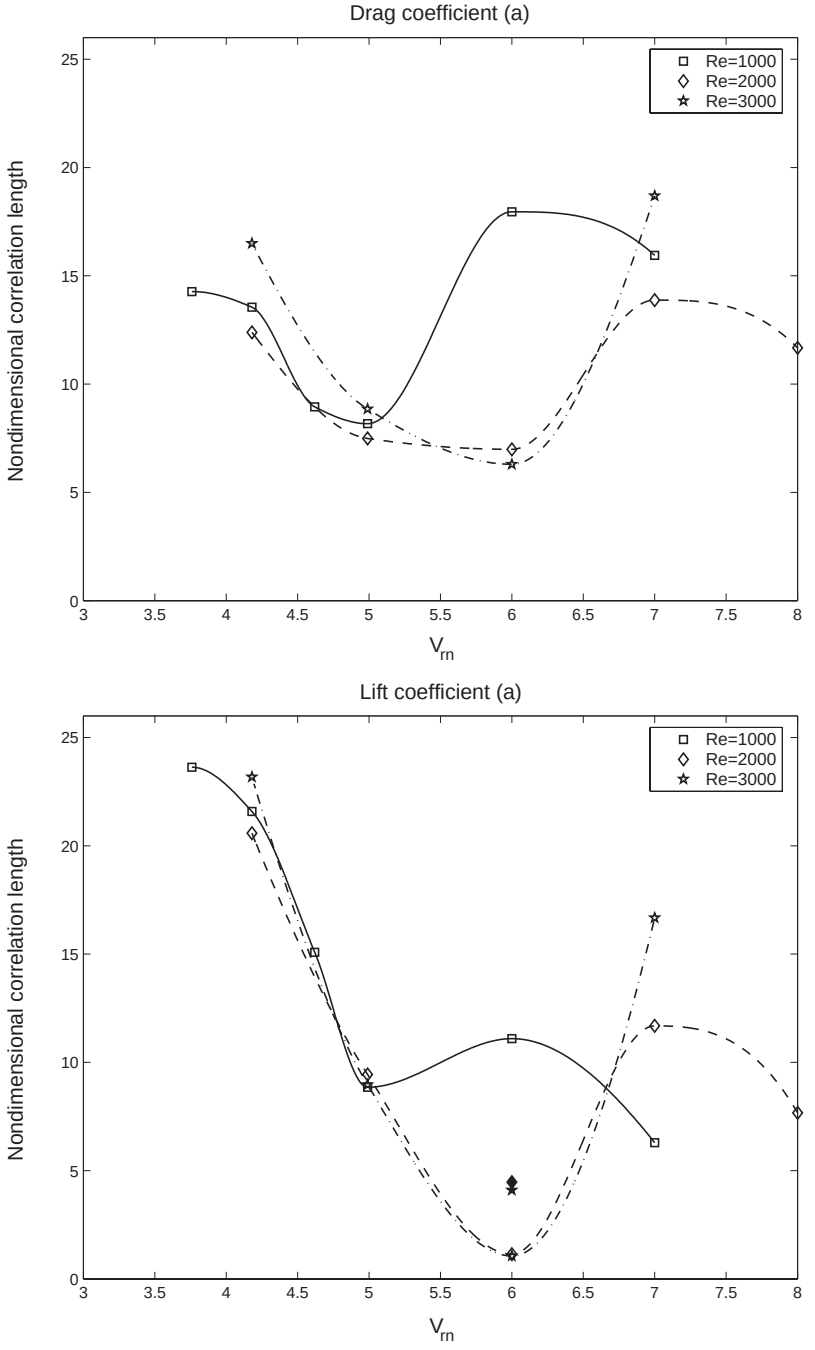

Fig. 18. Integrated drag and lift force coefficients correlation lengths (see Definition 3) from signals obtained with Method 1.

of a few cylinder diameters) for $V_{rn} = 6.00$, except for Re = 1000 where they reach a value of approximately 11 cylinder diameters. This is consistent with our previous hypothesis based on the complex demodulation results. The correlation lengths for $V_{rn} = 4.99$ exhibit strong modulations in time, but their mean values range similarly. The amplitude of the oscillation decreases somewhat with the Reynolds number. The order of the time period of the modulation is approximately 10 shedding cycles.

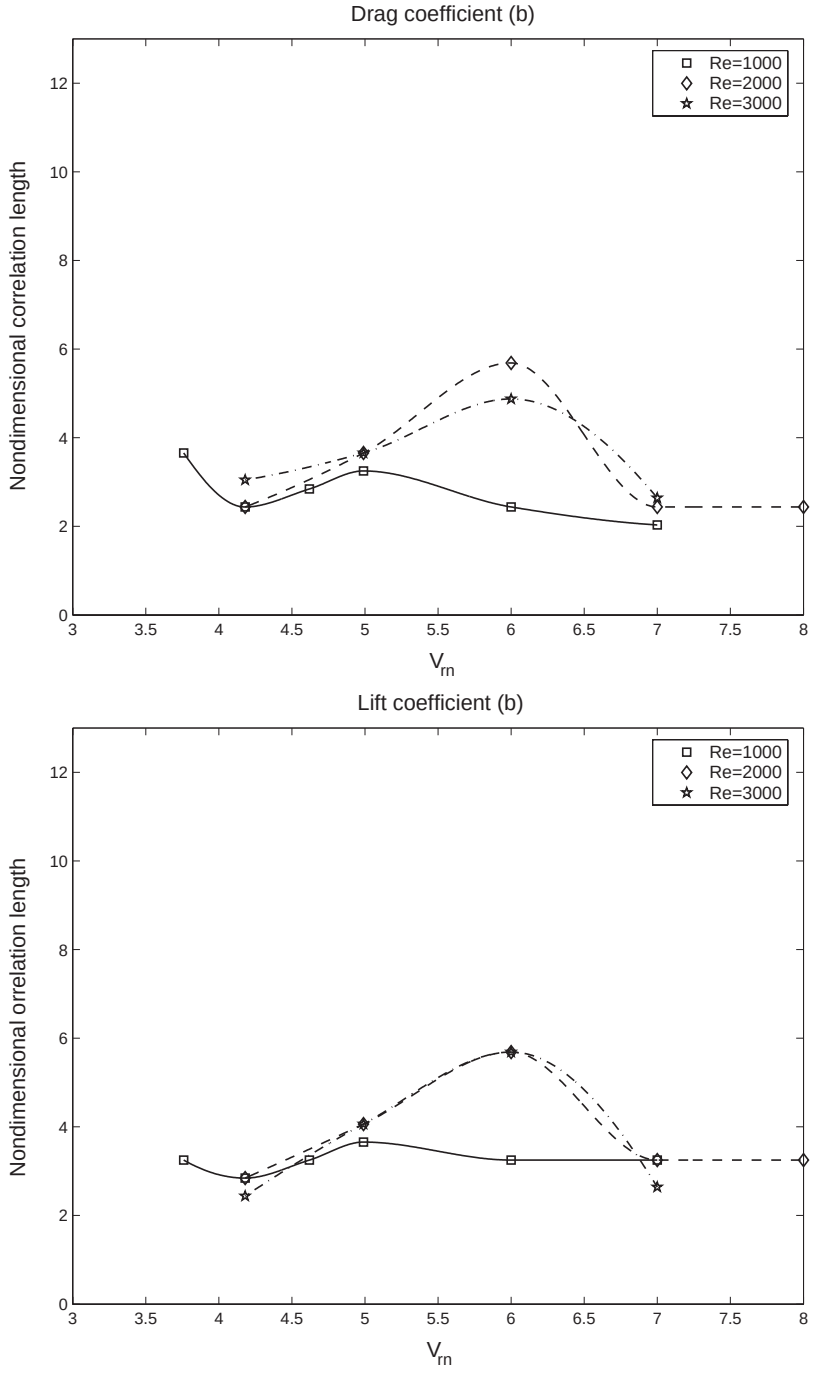

Fig. 19. Zero-crossing drag and lift force coefficients correlation lengths (see Definition 2) from signals obtained with Method 2.

6. Summary

We presented DNS of uniform flow at Reynolds number Re = 1000, 2000 and 3000 past a rigid cylinder with low mass-damping (zero structural damping) subject to VIV. We investigated different nominal reduced velocities within the synchronized region.

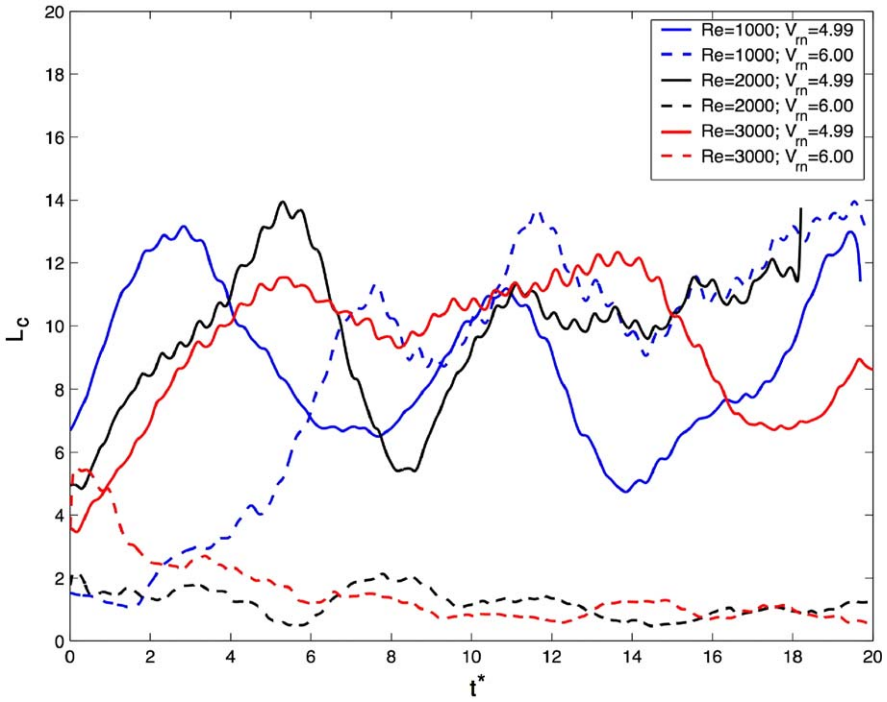

Fig. 20. Time traces of correlation lengths L_C of lift coefficient. Solid lines correspond to a reduced velocity $V_{rn} = 4.99$ and dashed lines correspond to $V_{rn} = 6.00$.

(i) obtained cylinder response results in good agreement with the "three-branch response" model proposed in experimental works. In particular, we confirmed the existence of an upper branch with large amplitude response. However, the width and magnitude of this upper branch is Reynolds number dependent. Indeed, some significant differences were obtained between the $\mathrm{Re} = 1000$ and $\mathrm{Re} = 2000-3000$ cases. As pointed out by Sarpkaya (2004), this illustrates the difficulty of interpreting experimental results where the reduced velocity is varied by means of a change in incoming inflow velocity (and not cylinder mass), which in turn induces a change in Reynolds number.
(ii) We observed a *stable* 2P vortex shedding mode in the lower branch region by performing two- and three-dimensional flow visualizations of the near wake as well as frequency analysis of the cylinder response and the velocity field.

We focused, in particular, on the reduced velocities around the transition between the upper and lower branch responses. We performed complex demodulation analysis of the phase difference between structural displacements and forces, and we also computed the correlation length of forces along the cylinder.

(a) We confirmed that there exists a reduced velocity range, near the mode transition from the *upper* to the *lower* hysteretic branch, and very close or including the Strouhal frequency, for which a severe drop in the spanwise correlation of the forces is observed.
(b) In this region of poor correlation, the topology of the vorticity in the wake is very complex and consists of multiple irregular cells inducing forces that are not in phase with each other. The complex demodulation analysis shows that regions of low lift force coincide with regions of poor phasing. Large forces exist where the phase difference between cylinder displacement and lift force is close to zero.
(c) The wake does not switch episodically from one mode (with a good phasing) to another mode (with a poor phasing) across the entire span. It also does not transition progressively and continuously with increasing reduced velocity, by passing through the entire range of phase angles from 0 to π. Instead, there exist two unique regions, with phase differences of 0 and π, that *coexist* instantaneously along the span. The position and shape of these two regions vary in time, implying that if vorticity-splits exist, their spanwise locations must change in time. This behavior differs

from that observed for forced oscillations of rigid cylinders subject to shear flows (Lucor and Karniadakis, 2004). The location and extent of the upper branch and the region of poor correlation both exhibit a Reynolds number dependency in the range 1000–3000.

Acknowledgements

This work was supported by the Office of Naval Research under the supervision of Dr T. Swean. Jasmine Foo would like to acknowledge the support of the DOE Computational Science Graduate Fellowship and Krell Institute. Computations were performed on the IBM SP4 and SGI Origin 3000 at DoD's supercomputing centers (NAVO, ERDC and ARSC).

References

Blackburn, H., Govardhan, R., Williamson, C., 2000. A complementary numerical and physical investigation of vortex-induced vibration. Journal of Fluids and Structures 15, 481–488.

Blackburn, H., Henderson, R., 1999. A study of two-dimensional flow past an oscillating cylinder. Journal of Fluid Mechanics 385, 255–286.

Bloomfield, P., 1976. Fourier Analysis of Time Series: an Introduction. Wiley, New York.

Evangelinos, C., 1999. Parallel simulations of VIV in turbulent flow: linear and non-linear models. Ph.D. Thesis, Division of Applied Mathematics, Brown University.

Evangelinos, C., Karniadakis, G., 1999. Dynamics and flow structures in the turbulent wake of rigid and flexible cylinders subject to vortex-induced vibrations. Journal of Fluid Mechanics 400, 91–124.

Govardhan, R., Williamson, C., 2000. Modes of vortex formation and frequency response of a freely vibrating cylinder. Journal of Fluid Mechanics 420, 85–130.

Hover, F.S., Davis, J.T., Triantafyllou, M.S., 2004. Three-dimensional mode transition in vortex-induced vibrations of a circular cylinder. European Journal of Mechanics B/Fluids 23, 29–40.

Hover, F., Techet, A., Triantafyllou, M., 1998. Forces on oscillating uniform and tapered cylinders in crossflow. Journal of Fluid Mechanics 363, 97–114.

Karniadakis, G., Orszag, S., 1993. Nodes, modes and flow codes. Physics Today, March, 34–42.

Karniadakis, G., Sherwin, S., 1999. Spectral/hp Element Methods for CFD. Oxford University Press, Oxford.

Khalak, A., Williamson, C., 1999. Motions, forces and mode transitions in vortex-induced vibrations at low mass-damping. Journal of Fluids and Structures 13, 813–851.

Lucor, D., 2004. Generalized polynomial chaos: applications to random oscillators and flow–structure interactions. Ph.D. Thesis, Brown University.

Lucor, D., Foo, J., Karniadakis, G., 2003. Correlation length and force phasing of a rigid cylinder subject to VIV. In: Benaroya, H., Wei, T. (Eds.), IUTAM Symposium on Integrated Modeling of Fully Coupled Fluid Structure Interactions Using Analysis, Computations and Experiments. Kluwer, Dordrecht, pp. 187–199.

Lucor, D., Karniadakis, G., 2004. Predictability and uncertainty in flow–structure interactions. European Journal of Mechanics/B Fluids 23/1, 41–49.

Mansy, H., Yang, P.-M., Williams, D., 1994. Quantitative measurements of three-dimensional structures in the wake of a circular cylinder. Journal of Fluid Mechanics 270, 277–296.

Meneghini, J., Bearman, P., 1995. Numerical simulation of high amplitude oscillatory flow about a circular cylinder. Journal of Fluids and Structures 9, 435–455.

Ribeiro, J., 1992. Fluctuating lift and its spanwise correlation on a circular cylinder in a smooth and in a turbulent flow. Journal of Wind Engineering and Industrial Aerodynamics 40, 179–198.

Sarpkaya, T., 2004. A critical review of the intrinsic nature of vortex-induced vibrations. Journal of Fluids and Structures 19, 389–447.

West, G., Apelt, C., 1993. Measurements of fluctuating pressure and forces on a circular cylinder in the Reynolds number range 10^4 to 2.5×10^5. Journal of Fluids and Structures 7, 227–244.

Williamson, C.H.K., Govardhan, R., 2004. Vortex-induced vibrations. Annual Review of Fluid Mechanics 36, 413–455.